Physics of the Earth and Planetary Interiors 352 (2024) 107212

Contents lists available at ScienceDirect

Physics of the Earth and Planetary Interiors

journal homepage: www.elsevier.com/locate/pepi

Seismic evidence for possible entrainment of rising plumes by subducting slab induced flow in three subduction zones surrounding the Caribbean Plate

Morvarid Saki [a,*], Sara Aniko Wirp [c,a], Magali Billen [b], Christine Thomas [a]

[a] Institute of Geophysics, University of Münster, Münster, Germany
[b] Earth and Planetary Sciences, UC DAVIS, University of California, California, USA
[c] GEOMAR, Helmholtz-Zentrum für Ozeanforschung, Kliel, Germany

ARTICLE INFO

Keywords:
Mantle transition zone discontinuities
PP and SS precursors
Caribbean subduction
Plume-slab interaction

ABSTRACT

The dynamic processes associated with subducting tectonic plates and rising plumes of hot material are typically treated separately in dynamical models and seismological studies. However, various types of observations and related models indicate these processes overlap spatially. Here we use precursors to PP and SS reflecting off mantle transition zone discontinuities to map deflections of these discontinuities near three subduction zones surrounding the Caribbean Plate: 1) Lesser Antilles, 2) Middle America and 3) northern South American subduction zones. In all three regions slow seismic anomalies are present behind the sinking slab within the transition zone in tomographic images. Using array methods, we identify precursors and verify their in-plane propagation for $M_W \geq 5.8$ events occurring between the years 2000 and 2020 by generating a large number of source receiver combinations with reflection points in the area, including crossing ray paths. The measured time lag between PP/SS arrivals and their corresponding precursors on robust stacks are used to measure the depth of the mantle transition zone discontinuities. In all three areas we find evidence for upward deflection of the 660 discontinuity behind the sinking slab, consistent with the presence of hot plume material (average temperature anomalies of 180 to 620 K), while there is not a corresponding downward deflection of the 410 km discontinuity. One interpretation of these disparate observations is suggested based on comparison to existing models of mantle convection and subduction: plume material rising across 660 km discontinuity could be entrained by lateral flow in the transition zone induced by the nearby sinking slab, and thus delaying the rise of hot material across the 410 km discontinuity.

1. Introduction

The subduction of lithospheric plates provides the primary source of negative buoyancy driving mantle and plate motions (e.g., Conrad and Lithgow-Bertelloni, 2002; Enns et al., 2005; Weller et al., 2019). High resolution tomographic images of subducting slabs indicate some slabs sink directly into the lower mantle, e.g., beneath Peru, the Marianas and Central America (van der Hilst et al., 1997; Fukao and Obayashi, 2013), while some others bend, or flatten out in response to the phase changes and corresponding increase in viscosity at 660 km, e.g., beneath the Izu-Bonin region or South-Kurile region (e.g., Isacks and Molnar, 1971; van der Hilst et al., 1991; Grand et al., 1997; Gudmundsson and Sambridge, 1998; Li et al., 2008; Hayes et al., 2012). In addition to the dynamical effects of the phase transitions, sinking slabs can also be affected by flow in the mantle caused by other sinking slabs (e.g., Jagoutz et al., 2015; Zhang et al., 2017; Pusok and Stegman, 2019), by large-scale mantle flow (e.g., Lee and King, 2011) and plumes rising from the lower mantle (e.g., Gurnis et al., 2000; Obrebski et al., 2010; Schmerr et al., 2010).

In this study, we map the topography of the mantle transition zone (MTZ) discontinuities beneath the subduction zones surrounding the Caribbean Plate using precursors to PP and SS waves reflecting at the underside of the upper mantle discontinuities. Precursors to PP and SS waves have been previously used to map regional (Rost and Weber, 2002; Schmerr and Thomas, 2011; Saki et al., 2015, 2019, 2022; Yu et al., 2017) and global discontinuity depths (e.g., Deuss, 2009; Deuss and Woodhouse, 2002; Lawrence and Shearer, 2006; Houser et al.,

* Corresponding author.
E-mail address: msaki_01@uni-muenster.de (M. Saki).

https://doi.org/10.1016/j.pepi.2024.107212
Received 16 May 2023; Received in revised form 12 March 2024; Accepted 14 May 2024
Available online 16 May 2024

2008; Flanagan and Shearer, 1998, 1999). Unlike other methods, they are sensitive to the reflection points at midway between source and receiver and are therefore independent of the availability of stations in the target region. Our main focus is on three major subduction zones (Fig. 1): 1) Lesser Antilles (LA, region 1) where the north and south American plates subducts under the Caribbean plane 2) Central America (CA, region 2) where the Cocos plate subducts under the north American and Caribbean plates beneath Mexico and Guatemala, and 3) South America (SA, region 3) where the Nazca plate subducts under the South America plate beneath Columbia and Ecuador.

Subduction in the Caribbean region has been imaged with seismic methods, such as tomography. The results by Fukao and Obayashi (2013) show the Cocos plate subducting under North and Central America to a depth of 660 km, perhaps even reaching the depth of ~1000 km. P-wave tomography of the Lesser Antilles slab indicates that although seismicity only extends to ~200 km the slab itself extends into the transition zone, with possibly detached and actively tearing regions of the slab (e.g., van der Hilst and Mann, 1994; Bezada et al., 2010; Harris et al., 2018; Allen et al., 2019; Brazus et al., 2021; Cornthwaite et al., 2021). As the resolution of tomographic imaging varies strongly depending on the combination of sources and receivers used (e.g., Barklage et al., 2015; Zhao et al., 2017) and degrades with increasing depth, only large-scale velocity structures within the deeper Earth can be interpreted confidently (Lu and Grand, 2016). Other studies have probed the upper mantle structure beneath the Caribbean plate with other types of observations and models, including gravity anomalies (e.g., Sanchez-Rojas and Palma, 2014; Syracuse et al., 2016; Schlaphorst et al., 2017), seismic anisotropy data (Lynner and Long, 2013; Porritt et al., 2014), and surface wave tomography (e.g., Miller et al., 2009; Durand et al., 2017) but the depth extent is often much shallower than body wave tomography studies.

An additional method to test the depth extent and path of subduction is the detailed analysis of MTZ seismic discontinuities. These seismic discontinuities are caused by solid-state phase transformations in the mantle minerals (mainly olivine and pyroxenes). The exact depth and width of these phase transitions depend on the mantle adiabat as well as the composition (e.g., (e.g., aluminum, calcium or iron content; Wood, 1995; Stixrude, 1997; Weidner and Wang, 1998). Equilibrium models of mineral assemblage tend to predict narrow transitions, on the order of kilometers (Stixrude and Lithgow-Bertelloni, 2011), while seismic observations tend to require broader transition widths (Helffrich, 2000). The seismic discontinuity located at approximately 410 km depth is due to the exothermic phase transformation from olivine to wadsleyite (Helffrich, 2000; Shim et al., 2001; Fei et al., 2004; Katsura et al., 2004; Frost, 2008). The 660 km discontinuity is primarily due to the endothermic transition of ringwoodite to bridgmanite and ferro-periclase (Ito

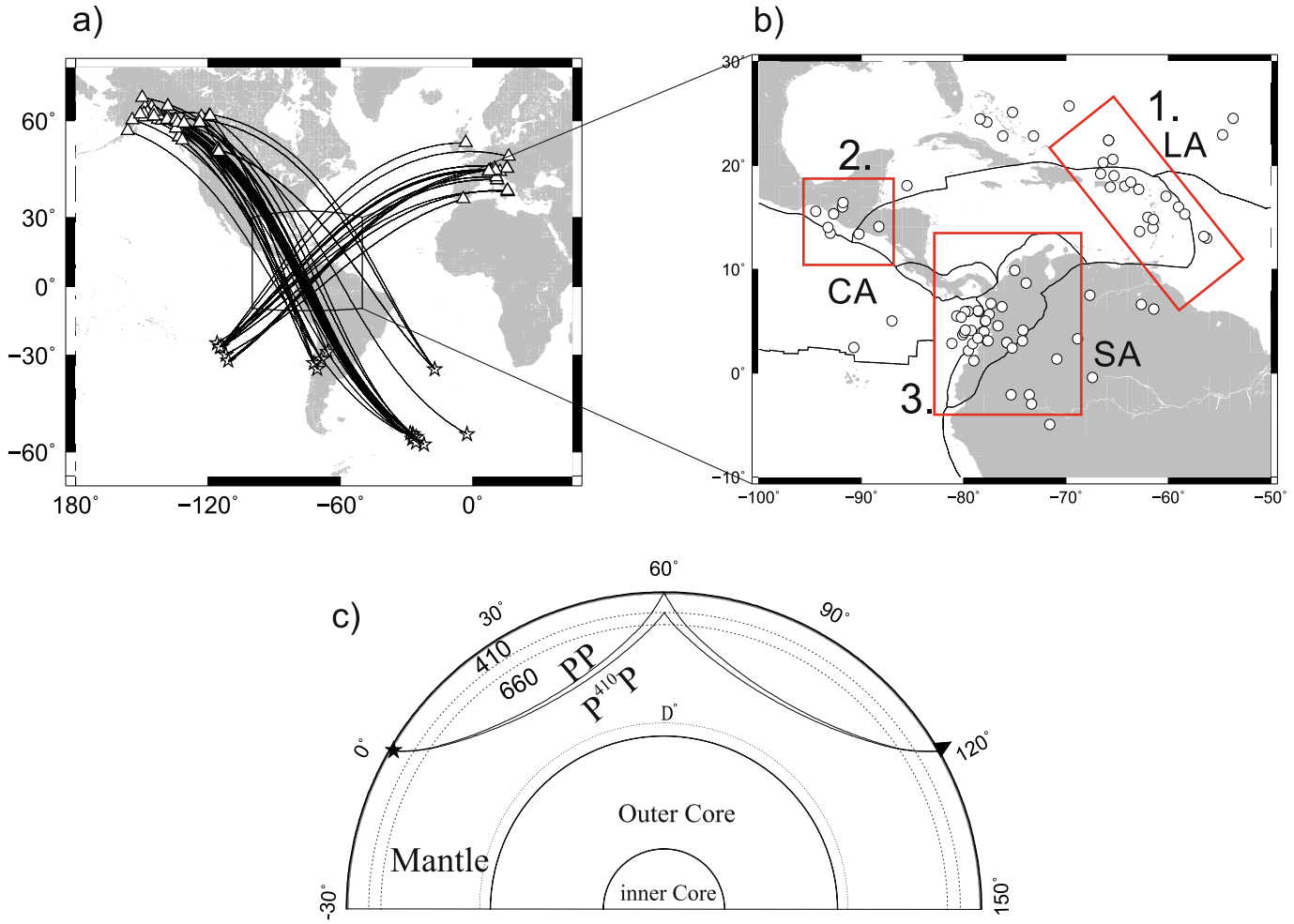

Fig. 1. (a) Source-receiver combinations used in this study. Stars and triangles represent the location of the events and central station of each bin, respectively. The great circle path for each source-receiver combination is shown by the solid lines. (b) Location of underside reflection points. Region 1: Lesser Antilles (LA) where the north and south American plates subduct under the Caribbean plate, region 2: Central America (CA), where the Cocos plate subducts under the north American and Caribbean plates beneath Mexico and Guatemala, and Region 3: South America (SA), where the Nazca plate subducts under the South America plate beneath Columbia and Ecuador. (c) Example ray paths of the waves used here, for simplicity only the PP and $P^{410}P$ ray paths are shown. The $P^{660}P$ wave travels along a similar ray path as PP but reflects at the underside of the 660 km discontinuity.

and Takahashi, 1989; Shim et al., 2001; Fei et al., 2004) although at some temperatures intermediate transitions to ilmenite (cold slab) or garnet (hot plumes) phases may also occur (see phase diagrams in Weidner and Wang, 1998 and Stixrude and Lithgow-Bertelloni, 2011).

To first order, deflections of the seismic discontinuities are interpreted in terms of thermal anomalies moving across these boundaries – colder slabs or hotter plumes. In this case, the magnitude of the deflection depends on the Clapeyron slope for the phase transition and can be used to estimate the thermal anomaly. In this simple interpretation, due to the opposite sign of the Clapeyron slopes of the phase changes occurring at 410 and 660 km boundaries, the depth variation of these two discontinuities are anticorrelated in response to the same thermal anomaly, potentially leading to a thinner than normal mantle transition zone thickness beneath hotspots and thicker than normal across subducting plates (Helffrich, 2000).

The simple interpretation of discontinuity deflection in terms of temperature alone does not account for: 1) differences in the phase transitions that occur at different temperatures, and 2) effects of bulk mineralogy (see summary in Thomas and Billen, 2009). Water content of the mantle may also influence the depth of the phase transition occurring at the 410 discontinuity (e.g., Helffrich, 2000; van der Meijde et al., 2003). Here we do not consider this for simplicity but note that there may be an effect. Seismic observations, are consistent with the primarily thermal dependence of the olivine to wadsleyite transition, but sometimes require a more complicated dependence for phase transitions occurring near 660 km depth (e.g., Deuss et al., 2006; Andrews and Deuss, 2008; Deuss, 2009; Thomas and Billen, 2009). Therefore, here we will use seismic tomography to provide additional information about the regional seismic wave speeds to provide more robust interpretations of observations.

Knowledge of the thermal anomalies crossing the mantle transition zone can provide strong constraints on the style of mantle convection (e.g., heat and material flux) which further aids in the interpretation of seismic images in terms of past plate motions (Shearer and Masters, 1992; Schubert and Tackley, 1995; Thomas and Billen, 2009; Fukao and Obayashi, 2013). Specifically, the positive Clapeyron slope for the olivine to wadsleyite transitions enhances the density anomaly due to temperature and thus aiding subduction or the ascent of a plume. In contrast, the negative Clapeyron slope for ringwoodite to bridgmanite plus ferro-periclase reduces the net density difference across the phase change boundary. These added density effects together with changes in viscosity across the phase changes can lead to complex behavior of both slabs (Arredondo and Billen, 2017) and plumes (Liu and Leng, 2019; Wamba et al., 2023) in the mantle transition zone.

2. Data and processing

We used broad-band velocity seismograms for several source-receiver combinations, which provided reflection points beneath the Caribbean and surrounding subduction zones (Fig. 1). Data were downloaded from the Incorporated Research Institutions for Seismology (IRIS) for the events occurring between 2000 and 2020 with magnitude of Mw $\geq$ 5.8 and no depth restriction. Events were collected within the epicentral distance range of 80 to 160° to ensure strong reflection amplitudes from the mantle transition zone boundaries and only few interfering waves (e.g., Flanagan and Shearer, 1998; Deuss, 2009).

For each array, seismograms of each event were visually inspected to determine the quality of the PP/SS waves: noisy data and events with fewer than 7 stations in an array were disregarded. Noise was measured in a window of 50 s length between 70 and 20 s before the P wave arrival and the window for the signal is 50 s around PP (SS). Only events with signal-to-noise-ratio >1.5 were kept. The events fulfilling these requirements were further analyzed, which led to 38 measurements as the final dataset used in this study (Table S1). It should be noted that the majority of the data had a much larger signal-to-noise-ration than 1.5.

The final dataset included source-receiver combinations that span two main directions. The first and dominant propagation path is SE-NW direction with earthquakes in South Atlantic recorded in North America and Alaska. The second source-receiver group are events from the South Pacific recorded in Europe, presenting an SW-NE direction (Fig. 1). These two paths sample our investigation area with crossing ray paths providing better resolution of the mantle transition zone discontinuities. As some of the arrays are very large and coherency may decrease across large arrays, we divided the array stations into bins and each bin contained stations within a radius of 300 km around the central station of the array to ensure coherency of the waves.

We analyzed the dataset using seismic array methods (e.g., Rost and Thomas, 2002; Schweitzer et al., 2002) to enhance the visibility of the precursors and to distinguish precursors by their slowness. Following the selection of events, we searched for PP and SS precursors caused by the reflection at the underside of seismic discontinuities in the MTZ (Fig. 1.c). The amplitude of these precursor signals is only a few percent of the waves reflected off the surface (e.g., Flanagan and Shearer, 1998; Flanagan and Shearer, 1999; Deuss, 2007, 2009; Schmerr and Garnero, 2007; Schmerr and Thomas, 2011; Lessing et al., 2015; Saki et al., 2015, 2019, 2022; Reiss et al., 2017) and precursor signals can coincide in arrival time with other phases such as PKIKP (e.g., Lessing et al., 2015). Therefore, as a first step, we stacked the data to generate 4th root vespagrams (Davies et al., 1971; Muirhead and Datt, 1976; Rost and Thomas, 2002) which allowed for the detection of PP/SS underside reflections by comparing the observed travel times to the theoretical travel time predicted by ak135 velocity model (Kennett et al., 1995). It also helped us to assess the slowness of the precursor, which should be close to the slowness of the main phase (PP or SS). After the detection of the precursors in the vespagram, the slowness-backazimuth analysis was used to confirm whether the signal was indeed a precursor signal by ensuring their in-plane arrival and correct slowness. Using the slowness-backazimuth analysis we were able to recognize and avoid the out-of-plane waves which may yield misleading results of reflector depths (Rochira and Thomas, 2023).

Fig. 2 and Fig. S1 show vespagram examples of precursor signals from the 410 km and 660 km discontinuity. The vespagrams show clearly separated PP and/or SS precursor from other arrivals such as PKIKP or Pdiff/Sdiff coda waves. It should be noted that the events with visible reflections from both 410 and 660 km discontinuities in the same vespagram are rare in our observations, as they have been in other studies (e.g., Thomas and Billen, 2009; Lessing et al., 2014; Saki et al., 2015). The non-detection of the reflections from the 660 km discontinuity in global stacks has been attributed to the reduced P-wave velocity contrast across the 660 km discontinuity compared to that given in global models such as ak135 (Kennett et al., 1995) or PREM (Dziewonski and Anderson, 1981). Alternatively, local variations of mineralogy at the 660 km discontinuity could potentially yield variable travel times of the precursors that would result in reduction of amplitude in the stacking process (Deuss, 2009).

We applied a range of filters to each broad-band seismogram section to find the filter providing the best visibility of the precursors. Bandpass filters with the corner periods between 1 s and 100 s were tested and we found that a butterworth bandpass filter with corner periods between 5 and 25 s provided clear arrivals of PP waves, while a butterworth bandpass filter with corner periods of 10 to 100 s was the best filter for detecting the SS waves in our dataset (Table S1). While we only used one filter for each wave-type, investigating the effect of different frequency filtering on the presence/absence of the precursor signals would potentially allow to understand sharpness of the discontinuity, and this is planned for a follow-up study.

Since the precursors propagate on a very similar path to the PP/SS waves reflected off the surface (Fig. 1.c), the differential travel time between precursor and main phase (PP/SS) can be converted to the depth of the discontinuity using the TauP toolkit (Crotwell et al., 1999) and ak135 velocity model. To estimate the depth uncertainty in our measurements, we used a bootstrap method, replacing the records

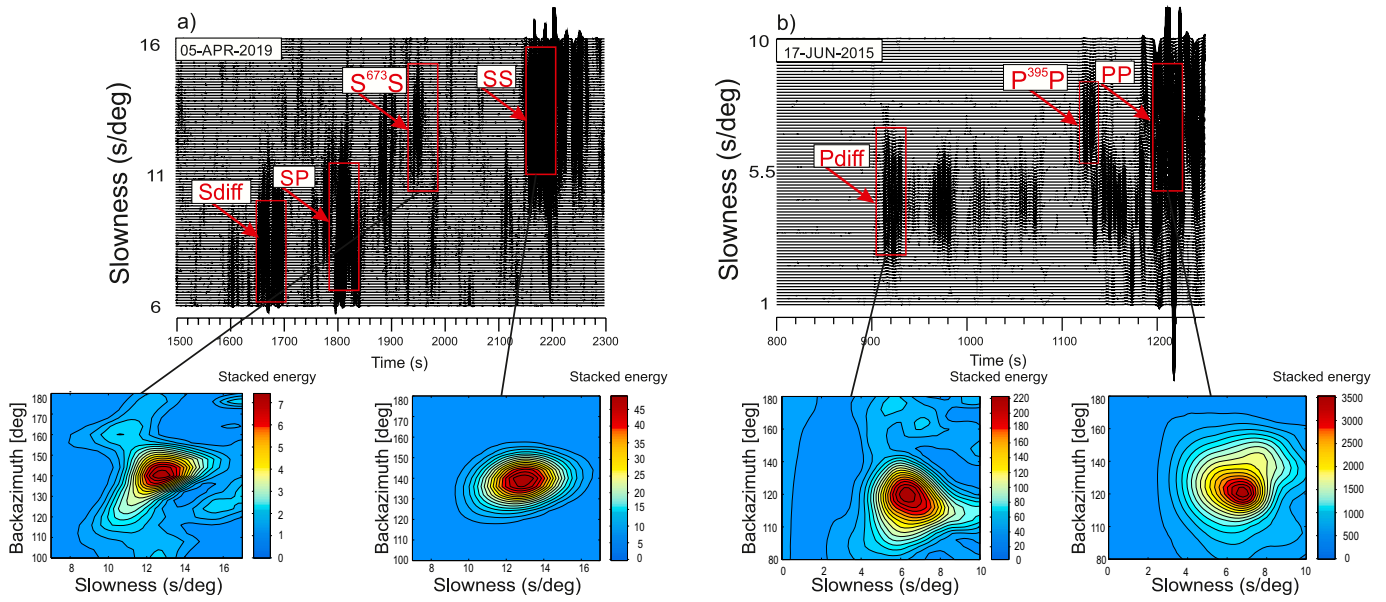

Fig. 2. 4th root vespagrams (Rost and Thomas, 2002) of different earthquakes for precursors to PP and SS waves and the corresponding slowness-backazimuth analysis in the bottom row. Examples of underside reflected waves (a) S wave reflected at 660 km discontinuity (depressed), (b) P-wave reflected at 410 km discontinuity (uplifted). The arrows point to the theoretical slowness values of different phases on the vespagram. Filters for the waves are given in Table S1.

randomly for 50 sets of traces and stacking them to produce a vespagram. We then measured the differential travel time between the precursor signal and the main phase (PP/SS) and converted them into depth ensuring the same part of the wavelet for PP/SS and precursor was used. The waves were corrected for mantle and crustal structure by using crustal model CRUST2.0 (Bassin et al., 2000) and the mantle tomography model MITP08 (Li et al., 2008) for P-waves and S40RTS (Ritsema et al., 2011) for S-waves. Finally, we calculated the mean depth value for each event from our 50 measurements per event and assigned this as the reflector depth, with the standard deviation as the measurement uncertainty (see Table S1).

The lateral resolution of the topography at the reflection points is governed by the large Fresnel zone of about 5–8 by 10–15 degrees (e.g., Deuss, 2009; Rost and Thomas, 2009) for P-wave and S-waves respectively, and small-scale variations of depth may be difficult to resolve from individual observations. (e.g., Deuss, 2009; Rost and Thomas, 2009). The use of arrays helps to decrease the size of the Fresnel zone (Rost and Thomas, 2009). Using synthetic data, Saki et al. (2022) showed that strong step-like topography of about 300 km (for example on a reflector at 1000 km, i.e., a step from 900 to 1200 km reflector depth) is still resolvable using array measurements, despite large Fresnel zones. Similarly, Lessing et al. (2015) tested the effect of topography of the 660 km discontinuity on the seismic wavefield and showed that a deflection would be detectable, but there would likely be a more complex waveform for the precursor, especially for a downward deflection. Still, variations in depth over small length-scales ($<5°$) should be taken with some caution (Saki et al., 2022).

We divided the observations into two different categories: for the majority of the events, due to high signal to noise ratio, the precursors showed very clear and clean signals (these events are shown with black borders of the symbols in Fig. 3), while for the remaining dataset the higher noise levels mean a less reliable pick of precursors and therefore larger errors in depth estimates (these events are marked with yellow borders of the symbols in Fig. 3). The calculated depth of the 410 km and 660 km discontinuities for each event and bin in our study area is shown in Fig. 3 and given in Table S1. The calculated depth of the 410 km discontinuity lies in the range of 382 $\pm$ 2.7 to 422 $\pm$ 4.2 km, while the 660 km discontinuity depth varies within 603 $\pm$ 3.6 to 703 $\pm$ 3.8 km.

We find that our reflection points are localized in three different regions: underneath the subduction zone of the Lesser Antilles (LA in Figs. 1 and 3), Central America (CA in Figs. 1 and 3) and the northwestern edge of South America (SA in Figs. 1 and 3). In the following, we will present results and discussion for each of those regions.

3. Results

3.1. Area 1 – Lesser Antilles

Due to the radiation pattern of events in the source region, the measurements for the 410 km discontinuity consist of mostly SS observations in the south and PP reflections further north, (area 1 in Fig. 3). The calculated depth for the 410 boundary indicates a change from elevated (shallower) depths beneath the south-eastern part of the subduction zone, moving to slightly depressed depths (5–10 km) towards the northwest. The four P-wave measurements agree with the depths from SS-precursors where they overlap spatially. The range in calculated depths of the 410 km discontinuity is up to 30 km in the area 1 box. Nearby observations lying outside of this box also indicate shallower than average depths (Fig. S2).

The observations of the 660 km discontinuity in this area indicate an uplifted discontinuity for most of the area, including a few reflection points outside the area 1 box in Fig. 3. The measurements for PP and SS precursors agree while some lower quality data (e.g., dark red circle outside box 1 also agree with high quality S-wave observations in the same place. The uplift of the discontinuity is around 20 km. Indeed, the 660 km discontinuity appears uplifted in all regions (Fig. 3d) as we will discuss.

Comparison of the observation points with the contours of the slab surface from the Slab 2.0 data set (Hayes et al., 2018) included in Fig. 3 and tomography models indicates that most of these observations likely sample the mantle underneath the sinking slab (e.g., tomography model DETOX, Hosseini et al., 2020, Fig. 4.b). The results of P-wave tomography of Harris et al. (2018) and van Benthem et al. (2013) find fast velocities to the west of our reflection points near 65 deg. W, with slower velocities in the region of our northern reflection area. Similarly, a compilation of tomography depth slices of the Lesser Antilles slab in a range of tomographic models (Mohammadzaheri et al., 2021) also shows the fast velocities towards the west and south-west of our reflection points. Comparing the tomographic results to the contours of Slab2.0 (Hayes et al., 2018) which only reach to a depth of

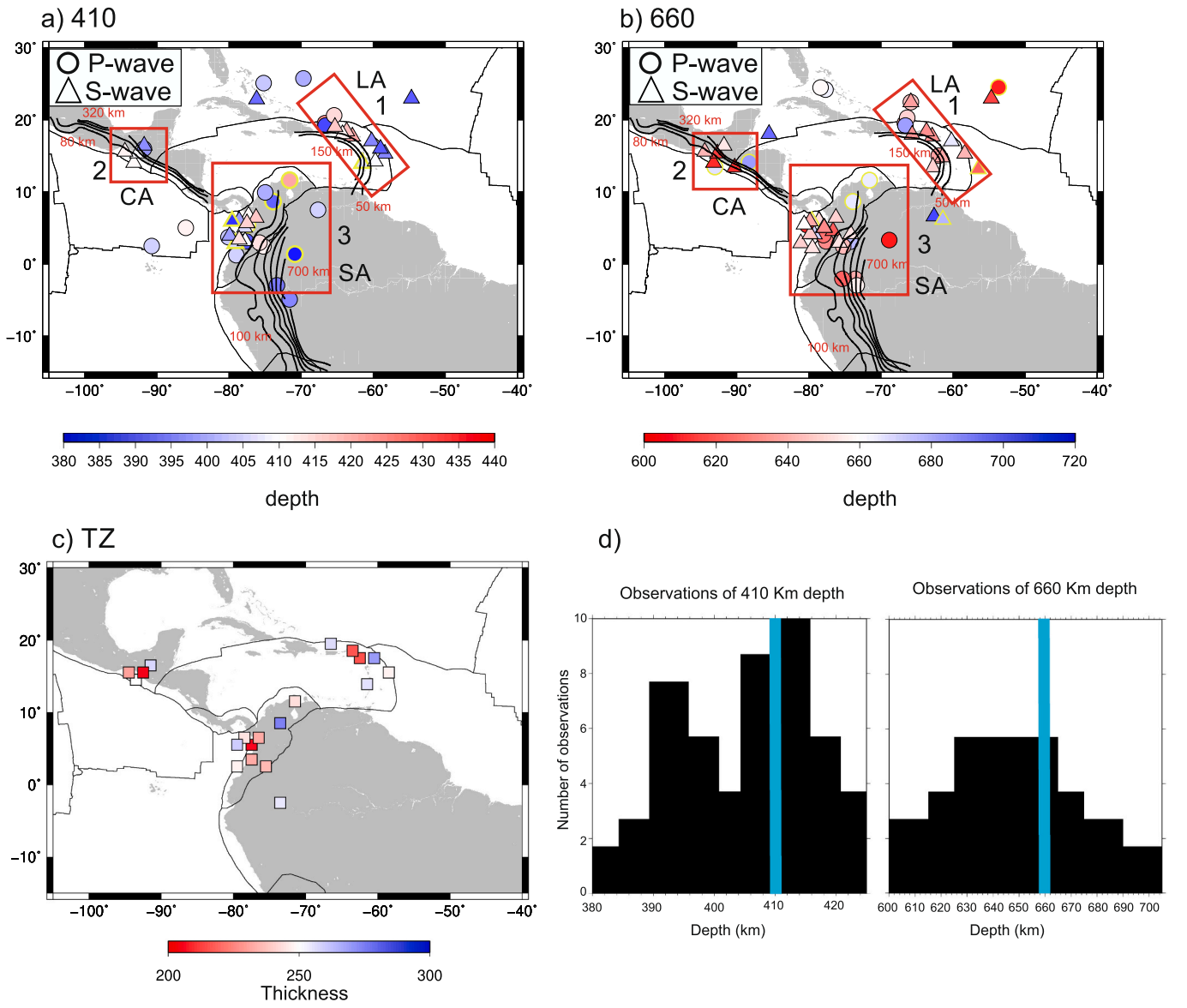

Fig. 3. Maps of the depth of 410 and 660 km discontinuities using precursors to PP (circles) and SS (triangles) waves. The high-quality observations, due to clear and clean data, are marked with a black border of the symbols. The yellow border of a symbol indicates that the result was obtained from data with higher level of noise. Solid black lines show the plate boundaries. (a) Results for the 410 km discontinuity depth. Reflection depths as given by the colour bar. Deeper reflections are indicated by red colours, shallower reflectors by blue colours. (b) Depth measurements for the 660 km discontinuity with colour indicating depth. Deeper reflectors are shown by blue colours, while red colour displays an elevated discontinuity. Slab contours (every 50 km for Lesser Antilles (LA, region 1), every 80 km for Central America (CA, region 2) and every 100 km for South America (SA, region 3) from Slab 2.0 (Hayes et al., 2018). c) Mantle transition zone thickness calculated by subtracting the estimated depths of the 410 km and 660 km discontinuities. d) Distribution of our depth measurements for the 410 and the 660 km discontinuities for the three regions in part a. (For interpretation of the references to colour in this figure legend, the reader is referred to the web version of this article.)

approximately 190 km for this region (Fig. S2), the trend of subduction is similarly towards the West, and Southwest, respectively, forming the curved- subduction imaged by tomography (Harris et al., 2018).

Therefore, based on the apparent dip of the slab and resolution of the tomographic models (e.g., DETOX, MITP08, S40RTS, Fig. 4 and Fig. S3), we estimate that even taking into account broadening of the slab thermal anomaly, these observations points do not directly sample the slab interior (Fig. S2, Fig. S3 and Fig. 4). For some parts of the region deflection of the 410 and 660 km discontinuities indicate a thinner transition zone (Fig. 3.c) consistent with anomalously warmer material flowing across both boundaries of the transition zone. However, in other regions, the 410 km appears unperturbed or shallow (blue) over regions with shallow depths (red) of the 660 km discontinuity. This suggest that a simple interpretation in terms of anomalously warm material rising across the mantle transition is not possible across the whole area and may indicate anomalously warm mantle rising underneath the colder sinking slab or just not reaching the top of the mantle transition zone. Tomographic images of DETOX (Hosseini et al., 2020) also show slower than average velocities east of the slab at 660 km depth (Fig. 4.b), supporting the possibility of warmer than average mantle material in the region of the reflection points at the 660 km discontinuity images (e.g., van Benthem et al., 2013; Hosseini et al., 2020).

3.2. *Area 2 – Central America*

Near the Mexican coast where the Cocos plate subducts under the North American continent (area 2, CA in Fig. 3) our observations consist of mostly SS observations and the number of reflection points is lower than in the other regions. Except for one dark blue triangle, the estimated depth of the 410 km discontinuity for the reflection points located

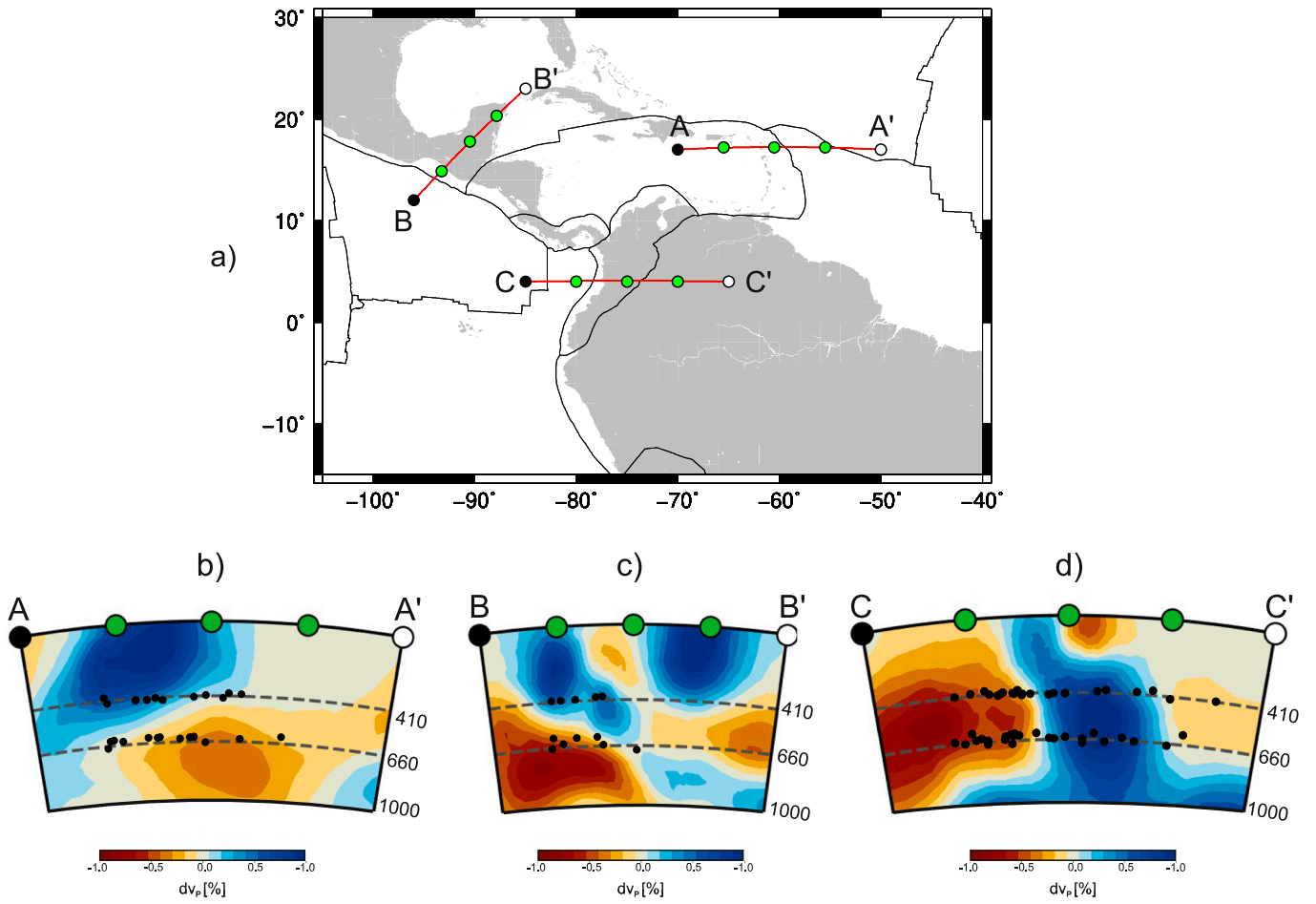

Fig. 4. a) Profiles through our investigation area and for LA (A-A'), CA (B—B)) and SA (C-C'). b-d) Depth slices through tomographic model DETOX (Hosseini et al., 2020) from the surface to 1000 km depth along the profiles A-A', B-B′ and C-C′ in (a) respectively. Black solid lines show the location of the slabs from Slab2.0 (Hayes et al., 2018) superimposed on each cross section. Black dashed lines mark the depths 410 km and 660 km. Black crosses are the single reflection depths.

near the subducting slab show little deviation from 410 km depth (white and light blue colours in Fig. 3a). However, the single observation furthest to the east shows an elevated 410 km discontinuity, as one would expect for the 410 km discontinuity influenced by a colder than normal mantle structure (e.g., Helffrich, 2000; Katsura and Ito, 1989; Katsura et al., 2004). Our observations agree with several other studies detecting an uplifted 410 km discontinuity in this region using other methods (e.g., joint inversion for mantle shear velocity and topography of transition zone discontinuities by Gu et al., 2003; observations of SP underside reflections by Reiss et al., 2018; observations of P wave receiver functions by Pérez-campos and Clayton, 2014). The location of the uplifted 410 km discontinuity also agrees with the location of the subducting Cocos plate in tomographic images (e.g., the DETOX model by Hosseini et al., 2020) shown in Fig. 4.c.

Observations of the 660 km discontinuity are mostly elevated (shallow by >20 km) except for one measurement underneath Mexico giving a depth of 666 km (Fig. 3). The upward deflected 660 km discontinuity in this region combined with slightly deflected 410 km discontinuity leads to a thinner than normal mantle transition zone thickness (Fig. 3.c). This shallower discontinuity depth is similar to studies by Flanagan and Shearer (1998) and Gu et al. (2003) who found elevated 660 by up to approximately 15 km in the same region. Based on comparison with the Slab 2.0 data (Fig. S2) set and tomography model DETOX (Hosseini et al., 2020) the eastern-most observation point (with elevated 410 and depressed 660 km) should lie within the slab (Fig. 4.c and Fig. S2). However, the other observations sample the mantle beneath the slab: in particular the observations of the 410 km discontinuity are well outside any thermal effect of the sinking slab. Similar to the Lesser Antilles, the observations of the deflections of the 410 km and 660 km discontinuities are not consistent with a simple interpretation in terms of warm material vertically rising across both boundaries of the mantle transition zone.

3.3. *Area 3 – Northwest coast of South America*

In the third region, near the north-western South American coast (area 3, SA in Fig. 3) we find depth values for the 410 km discontinuity ranging from normal depth (410 km) to mostly elevated depths (blue) with a shallowing of the discontinuity by up to 20 km. Here we have the largest number of reflection points from PP and SS precursors and, while there is scatter, the average for the entire region shows an elevated 410 km discontinuity. Comparison to the slab contours (Fig. 3.a) again indicates that none of the elevated depths are within the likely thermal halo of the underside of slab (distance of >200 km).

The 660 km discontinuity in this region shows a similar behavior, from normal to mostly elevated (shallow) depths throughout the area 3 (Fig. 3b,d), indicating likely hotter temperatures. Some measurements of deeper depth of the discontinuity are also found in the east of this investigation area and could coincide with the location of the slab at this depth, however these events did not display a reflection from the 410 km discontinuity. Following the path of subduction of the Colombia-Maracaibo slab in different P-wave tomographic images (van Benthem et al., 2013; Yarce et al., 2014; Hosseini et al., 2020; Portner et al., 2020; Mohammadzaheri et al., 2021) we confirm that slower than average

velocities are imaged where most of our reflection points sample the 660 km discontinuity (Fig. 4.d, Fig. S2 and Fig. S3). A low velocity anomaly surrounding the slab has also been detected by a joint inversion of seismic and gravity data beneath Colombia (Syracuse et al., 2016). Therefore, similar to the other two regions, we find an elevated 660 km discontinuity without a corresponding deeper 410 km discontinuity and thinner than normal MTZ thickness (Fig. 3.c), even though we are well away from the thermal effect of the slab at the top of the mantle transition zone for these reflection points.

4. Discussion

The observations indicate that in the Lesser Antilles, the 410 km discontinuity is elevated by up to 30 km in the south near the slab. In Central America, the 410 km is either unperturbed or elevated (one location). In South America, the 410 km is uplifted by up to 20 km. For the 660 km discontinuity we find elevated reflection points (up to 20 km) in the regions directly behind and under the Central America slab, most northerly section of the South America (Columbia) slab and the Lesser Antilles slab. In all three areas, comparison to tomographic images (Fig. 4) and the dip of the slab indicate that only a few of the reflection points are close enough to the slab to be affected by the cold slab temperatures. The good correspondence of these points with the location of the slab from seismicity and tomography provide confidence in our detection of discontinuity depths further away from the slabs.

The elevated 660 km discontinuities all appear to sample the mantle in regions with slow seismic anomalies located behind the slabs in several tomographic models (e.g., Fig. 4, Fig. S2 and Fig. S3). The large Fresnel zone does translate into sensitivity to structure over distances of hundreds of km, but previous studies have shown that step-like changes in discontinuity depth can still be confidently detected using array methods (Saki et al., 2022). Therefore, we conclude that the data do indicate elevated 660 km discontinuity in all three regions in the locations behind the slabs.

The simplest interpretation of the uplifted 660 km discontinuity is the presence of hotter than average mantle material rising across the base of the mantle transition zone. Using the observed deflection depths and Clapeyron slope (−2.5 Pa/K) for the ringwoodite to bridgmanite and ferro-periclase transition (Ye et al., 2014), we estimate that excess temperatures are 30 to 1000 K (see data sheet and Table S2 included in the Supplementary Material).

Deflections of the seismic discontinuities at 410 and 660 km differences relative to the average mantle at these depths are related to differences in temperature and major element composition, as well as concentration of water (Lebedev et al., 2002; Katsura et al., 2003; Fei et al., 2004; Litasov et al., 2005a, 2005b; Ishii et al., 2011; Kaneshima et al., 2012; Ghosh et al., 2013). For ringwoodite to bridgmanite and ferro-periclase transition (rw to brg + fp) the range in Clapeyron slope varies from −0.5 to −3.0 Pa/K: higher water concentration increases the Clapeyron slope, while increased iron decreases the Clapeyron slope. Larger values (e.g., −4 to −6 MPa/K) found in earlier experimental studies (e.g., Ito et al., 1989; Ito et al., 1990; Weidner and Wang, 1989) are no longer Weidner and Wang, 2000 as valid because improved experimental techniques (in particular better constraints on pressure), have shown that Clapeyron slopes are lower than those previous studies. In addition, calculations of equilibrium phase assemblages show that the Clapeyron slope varies with temperature, and also changes depending on whether the mantle is treated a single rock type (pyrolite) compared to a mixture of harzburgite and basalt (Stixrude and Lithgow-Bertelloni, 2011, 2012).

Given all these factors contributing to the depths of the phase transitions responsible for the major seismic discontinuities, we acknowledge that choosing a single Clapeyron slope values for estimating the potential temperature differences can only lead to first order interpretations. Here, we use a single intermediate value, weighing the higher values typical of seismic estimates more heavily than the smaller values coming from end-member composition experimental studies. However, if the true effective Clapeyron slope is substantially smaller, the observations would require larger plume temperatures making it more likely that such a plume would continue to rise up through the transition zone, which is not supported by the observations at 410 km. Future models incorporating plumes, slabs and the full equilibrium phase assemblage calculations are needed to provide more this analysis from a first order test of the hypothesis to a detail studied of potential trade-offs.

There are two possible explanations for warm thermal anomalies behind the subducting slabs. The first possibility is a local return flow caused by the sinking of the slab into the mantle. If such a flow exists it could advect warmer lower mantle material up into the transition zone. We reject this possibility for two reasons. First numerical models of subduction show that slabs sinking into the lower mantle lead to a broad region of entrained flow, which is also sinking downward into the mantle (Fig. 5). Because the viscosity of the lower mantle is >10 times higher than the average viscosity of the upper mantle, the flow is slower and broader in the lower mantle than in the upper mantle. Second, the large upward deflection of the 660 km discontinuity requires average temperature anomalies of 240–600 K– such large temperature differences are normally associated with fast rising plumes (Trela et al., 2017). Slower rising material will have more time to thermally equilibrate with the surrounding mantle making it difficult to maintain the large thermal anomalies required to match the observed deflections.

The second possibility is therefore actively upwelling hot (plume) material from the lower mantle. This possibility is consistent with the thermal anomaly required to match the height of the deflections at the 660 km discontinuity. However, the lack of a depressed 410 km discontinuity at the corresponding locations above these points indicates that the thermal anomaly is limited to the deeper part of the transition zone. This can be explained by accounting for the lateral deflection of the slab-induced flow caused by the sharp increase in viscosity at the base of the transition zone (Fig. 5). The viscosity contrast between the upper and lower mantle forces a partitioning of sinking slab induced flow into a lateral component of flow because the sinking rate decreases

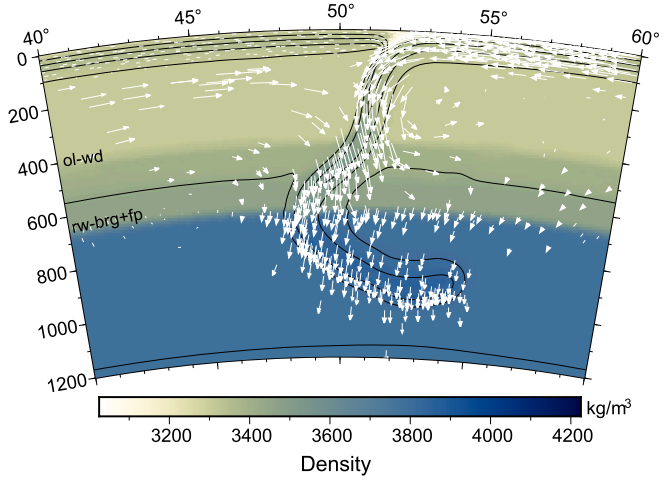

Fig. 5. Example of lateral flow behind the slab from a 2D simulation of subduction. Features to note: decrease in sinking rate of slab from top of transition zone to bottom of transition zone, and across the 660 km discontinuity. Rotation of flow behind the slab from nearly vertical to horizontal flow. This flow is typical during episodes of slab folding and roll-back. It is this flow that could push a rising plume laterally within the transition zone. Colour shows density due to temperature, composition and phase changes. Contours are temperature every 300 K from 600 to 2100. Arrows are scaled to magnitude of flow (maximum in upper mantle is 6.2 cm/yr; maximum in lower mantle is 2.0 cm/yr). Model set-up is similar to Billen and Arredondo (2018) but uses a domain width of 140° in longitude at equator (Weidner and Wang, 2000 et al., Weidner and Wang, 2000).

abruptly at the upper-lower mantle boundary (Arredondo and Billen, 2017; Billen and Arredondo, 2018). In addition, the flow in the asthenosphere is coupled to the sinking flow of the subducting plate and could therefore act to hinder further rise of the buoyant material out of the transition zone.

The ability of the slab-induced flow to stall a rising plume in the transition zone depends on the rate of rise of the plume relative to opposing flow. As an order of magnitude estimate, a Stokes sphere with radius of 100 km and temperature anomaly of 240 K rising through a mantle with viscosity of 1e21 Pa-s will have an upward velocity on the order of 1 cm/yr. However, the rising velocity increases proportional to the temperature anomaly, so a plume with a temperature anomaly of 600 K, would rise 2.5 times faster. Therefore, moderately buoyant plumes rising into the transition zone on either side of the slab could be both diverted laterally and hindered from rising further due to the slab induced flow in the surrounding mantle (Fig. 6).

One shortcoming of most subduction models is that they are focused on the evolution of slabs in an empty mantle (e.g., Arredondo and Billen, 2017). Larger-scale (but lower resolution) global mantle convection models demonstrate that heating of the lower mantle thermal boundary layers leads to upwellings on multiple scales, including plumes (McNamara and Zhong, 2004; Zhong., S., 2006; Tackley, 2012; Koppers et al., 2021). One interesting result from geodynamical models is the formation of smaller scale plumes at the base of the transition zone as the result of a larger scale upwelling and decrease in viscosity into the mantle transition zone (van Keken and Gable, 1995; Courtillot et al., 2003; Liu and Leng, 2019). The combination of this process of spawning multiple narrow plumes and the slab induced flow could explain the observations of a broad region of elevated 660 km discontinuity under/behind the slabs in these three regions.

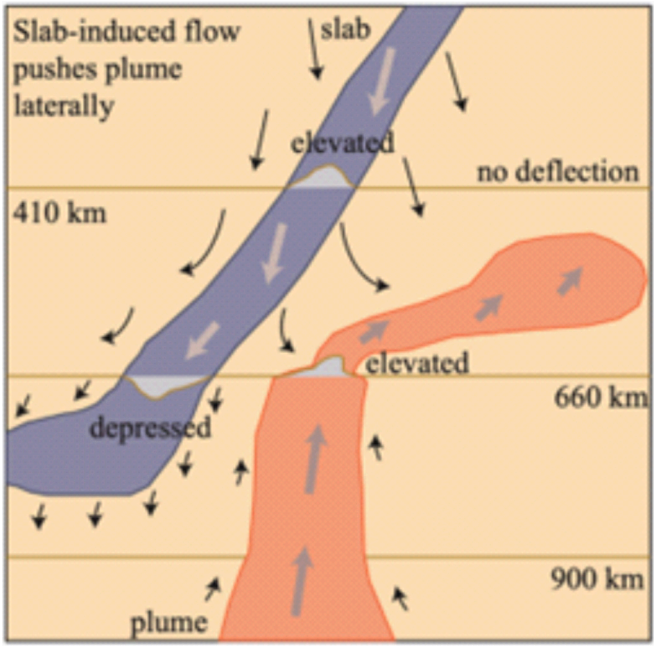

Fig. 6. Sketch illustrating possible interaction of a rising plume and sinking slab consistent with the observed deflections of the mantle transition zone discontinuities. Bold arrows show sinking or rising of the slab and plume. Thin black arrows show the mantle flow induced by the sinking slab and rising plume. Based on models of slab dynamics (example shown in Fig. 5), slab induced flow could both counter the rising of the plume and deflect it laterally depending on its distance from the slab and buoyancy of the slab. This could result in the observed upward deflection of the 660 km discontinuity behind the slabs, without an associated downward deflection of the 410 km discontinuity. Future studies could model this interaction and make forward models of both the expected tomographic image and discontinuity deflections for comparison with observations, and to understand the conditions (e.g., relative position of plume and slab; stage of subduction evolution, buoyancy of plume, role of phase changes and viscosity contrast), necessary to match the observations.

While robust counts of active plumes originating from the core-mantle boundary enumerate only 18 plumes (e.g., Koppers et al., 2021), this does not account for secondary plumes that may originate from a larger thermo-chemical plume, or substantially thinner, purely thermal plumes, which are difficult to image seismically (Courtillot et al., 2003; Koppers et al., 2021). From this perspective the possibility that there are active plumes rising in vicinity of sinking slabs is not so surprising. The interaction of rising plumes with slabs is not a new idea (see Table S3 included in the Supplementary Material) – however, it has been treated more as an anomalous occurrence (e.g., Yellowstone plume impinging on and breaking the Farallon slab, Obrebski et al., 2010; Samoa plume at the northern boundary of the Tonga-Kermadec slab, Chang et al., 2016), rather than a more normal component of plate tectonics in an actively convecting mantle. Indeed, for the South America slab beneath Columbia – the Galapagos plume lies just several 100 km to the southwest.

The interpretation of the discontinuity depths in terms of plumes rising up through the base of the mantle transition zone presented here uses simple scaling for interpreting the expected deflections of the discontinuities as well as the potential for slab-induced flow to stall and deflect the rising plume. To further test this interpretation, more seismological constraints on the length scale of the discontinuity deflections are needed and dynamical models exploring the interaction of different sized plumes with sinking slabs are needed to further test what sized plumes can be deflected by slab flow. Such models could provide important constraints on the viscosity contrast across the upper mantle transitions and the absolute value of viscosity within the transition zone.

Future models are needed to specifically model this process, as well as provide both the thermal models and phase transition depth within the secondary plumes so that these can be used to make synthetic seismic tomography models for comparison to seismic models. These seismic observations, therefore, call for development of a robust workflow connecting the results of dynamic models to creation of synthetic seismic models to further improve our understanding of transition zone dynamics.

5. Conclusions

The observations of an elevated 660 km discontinuity using seismological data array methods presented here provides another valuable data constraint indicating plume-slab interaction in three separate locations. These observations are complementary to seismic tomography observations as they are not subject to the same kinds of modeling uncertainties (but are subject to other errors as discussed), and to geochemical observations, because they can provide more specific spatial constraints on the location and extent of thermal anomalies. We conclude that similar analysis behind slabs in regions with slow seismic velocity anomalies would help to determine the global prevalence of such interactions and could in turn provide further constraints on material properties of the mantle (e.g., viscosity, effective Clapeyron slope) through geodynamical modeling of the interaction of rising plumes and sinking slabs.

Author agreement

All authors have seen and approved the final version of the manuscript being submitted. They warrant that the article is the authors' original work, hasn't received prior publication and isn't under consideration for publication elsewhere.

CRediT authorship contribution statement

Morvarid Saki: Formal analysis, Investigation, Methodology,

Visualization, Writing – original draft, Writing – review & editing. **Sara Aniko Wirp:** Formal analysis, Investigation, Methodology, Visualization. **Magali Billen:** Writing – review & editing. **Christine Thomas:** Conceptualization, Methodology, Project administration, Supervision, Writing – review & editing.

Declaration of competing interest

There is no conflict of interest.

Data availability

Data will be made available on request.

Acknowledgements

We would like to thank the editor and two anonymous reviewers for their detailed comments that greatly improved the manuscript. Data were downloaded from the Incorporated Research institute for Seismology (IRIS) and the Seismic Central Observatory (SZO) from Federal Institute for Geosciences and Natural Resources (BGR). Data analyses were performed with Seismic Handler (Stammler, 1993) and the Taup toolkit (Crotwell et al., 1999). Maps are generated using Generic Mapping Tools (Wessel and Smith, 1995). The work was supported by DFG grant TH1530/10-2 (MS) and TH1530/18-1. M. Billen thanks Sujoy Mukhopadhyay and Max Rudolph for their assistance in locating relevant plume observation literature. The subduction model depicted in Fig. 5 was run with the software Aspect (Bangerth et al., 2022) and provided by PhD student Haoyuan Li at UC Davis.

Appendix A. Supplementary data

Supplementary data to this article can be found online at https://doi.org/10.1016/j.pepi.2024.107212.

References

Allen, R.W., Collier, J.S., Stewart, A.G., Henstock, T., Goes, S., Rietbrock, A., the VoiLA Team, 2019. The role of arc migration in the development of the Lesser Antilles: a new tectonic model for the Cenozoic evolution of the eastern Caribbean. Geology 47, 891–895.

Andrews, J., Deuss, A., 2008. Detailed nature of the 660 km region of the mantle from global receiver function data. J. Geophys. Res. 1113 (B6).

Arredondo, K.M., Billen, M.I., 2017. Coupled effects of phase transitions and rheology in 2D dynamical models of subduction. J. Geophys. Res. 122, 5813–5830.

Bangerth, W., Dannberg, J., Fraters, M., Gassmoeller, R., Glerum, A., Heister, T., Myhill, R., Naliboff, J., 2022. ASPECT v2.4.0 (version v2.4.0). Zenodo. https://doi.org/10.5281/zenodo.6903424.

Barklage, M., Wiens, D.A., Conder, J.A., Pozgay, S., Shiobara, H., Sugioka, H., 2015. P and S velocity tomography of the Mariana subduction system from a combined land-sea seismic deployment. Geochem. Geophys. Geosyst. 16 (3), 681–704.

Bassin, C., Laske, G., Masters, G., 2000. The current limits of resolution for surface wave tomography in North America. EOS Trans. Am. Geophys. Union 81, F897.

Bezada, M.J., Levander, A., Schhmandt, B., 2010. Subduction in the southern Caribbean: images from finite-frequency P wave tomography. J. Geophys. Res. Solid Earth 115 (B12).

Billen, M.I., Arredondo, K.M., 2018. Decoupling of plate-asthenosphere motion caused by non-linear viscosity during slab folding in the transition zone. Phys. Earth Planet. Inter. 281, 17–30.

Brazus, B., Goes, S., Allen, R., Rietbrock, A., Collier, J., Harmon, N., Henstock, T., Hicks, S., Rychert, C.A., Maunder, B., van Hunen, J., Bie, L., Blundy, J., Vooper, G., Davy, R., Kendall, M., Macpherson, C., Wilkinson, W., Wilson, M., 2021. Subduction history of the Caribbean from upper-mantle seismic imaging and plate reconstruction. Nat. Commun. 12, 4211.

Chang, S.-J., Ferreira, A.M.G., Faccenda, M., 2016. Upper- and mid-mantle interaction between the Samoan plume and the Tonga–Kermadec slabs. Nat. Commun. 7 (10799), 1–9.

Conrad, C.P., Lithgow-Bertelloni, C., 2002. How mantle slabs drive plate tectonics. Science 298, 207–209.

Cornthwaite, J., Bezada, M.J., Miao, W., Schmitz, M., Prieto, G.A., Dionicio, V., Niu, F., Levander, A., 2021. Caribbean slab segmentation beneath Northwest South America revealed by 3-D finite frequency teleseimic P wave tomography. Geochem. Geophys. Geosyst. 22 (4).

Courtillot, V., Davaille, A., Besse, J., Stock, J.S., 2003. Three distinct types of hotspots in the Earth's mantle. Earth Planet. Sci. Lett. 205, 295–3083.

Crotwell, H.P., Owens, T.J., Ritsema, J., 1999. The Taup toolkit: flexible seismic travel-time and ray-path utilities. Seismol. Res. Lett. 70, 154–160.

Davies, D., Kelly, E.J., Filson, J.R., 1971. Vespa process for analysis of seismic signals. Nature 232, 8–13.

Deuss, A., 2007. Seismic observations of transition zone discontinuities beneath hotspot locations. Geol. Soci. America 430, 121–136.

Deuss, A., 2009. Global observations of mantle discontinuities using SS and PP precursors. Surv. Geophys. 30, 301–326.

Deuss, A., Woodhouse, J.H., 2002. A systematic search for mantle discontinuities using SS-precursors. Geophys. Res. Lett. 29 (8), 90-1 – 90-4.

Deuss, A., Redfern, S.A.T., Chambers, K., Woodhouse, J.H., 2006. The nature of the 660-kilometer discontinuity in Earth's mantle from global seismic observations of PP precursors. Science 311, 198–201.

Durand, S., Debayle, E., Ricard, Y., Zaroli, C., Lmabotte, S., 2017. Confirmation of a change in the global shear velocity pattern at around 1000 km depth. Geophys. J. Int. 211 (3), 1628–1639.

Dziewonski, A.M., Anderson, D.L., 1981. Preliminary reference earth model. Phys. Earth Planet. Inter. 25 (4), 297–356.

Enns, A., Thorsten, W.B., Schmeling, H., 2005. The dynamics of subduction and trench migration for viscosity stratification. Geophys. J. Int. 160 (2), 761–775.

Fei, Y., Orman, J.V., Li, J., Westrenen, W.V., Sanloup, C., Minarik, W., Hirose, K., Komabayashi, T., Walter, M., Funakoshi, K., 2004. Experimentally determined postspinel transformation boundary in Mg_2Sio_4 using MgO as an internal pressure standard and its geophysical implication. J. Geophys. Res. Solid Earth 109, B02305. https://doi.org/10.1029/2003JB002562.

Flanagan, M.P., Shearer, P.M., 1998. Global mapping of topography on transition zone velocity discontinuities by stacking SS precursors. J. Geophys. Res. Solid Earth 103, 2673–2692.

Flanagan, M.P., Shearer, P.M., 1999. A map of topography on the 410-km discontinuity from PP precursors. Geophys. Res. Lett. 26, 549–552.

Frost, D.J., 2008. The upper mantle and transition zone. Elements 4, 171–176.

Fukao, Y., Obayashi, M., 2013. Subduction slabs stagnant above, penetrating through, and trapped below the 660 km discontinuity. J. Geophys. Res. Solid Earth 118 (11), 5920–5938.

Ghosh, S., Ohtani, E., Litasov, K.D., Suzuki, A., Dobson, D., Funakoshi, K., 2013. Effect of water in depleted mantle on post-spinel transition and implication for 660 km seismic discontinuity. Earth Planet. Sci. Lett. 371-372, 103–111.

Grand, S.P., van der Hilst, R.D., Widiyantoro, S., 1997. Global seismic tomography: a snapshot of convection in the earth. GSA Today 7, 1–7.

Gu, Y.J., Dziewonski, A.M., Ekström, G., 2003. Simultaneous inversion for mantle shear velocity and topography of transition zone discontinuities. Geophys. J. Int. 154 (2), 559–583.

Gudmundsson, O., Sambridge, M., 1998. A regionalized upper mantle (RUM) seismic model. J. Geophys. Res. Solid Earth 103 (B4), 7121–7136.

Gurnis, M., Ritsema, J., Can Heijst, H.-J., Zhong, S., 2000. Tonga slab deformation: the influence of a lower mantle upwelling on a slab in a young subduction zone. Geophys. Res. Lett. 27 (16), 2373–2376.

Harris, C.W., Miller, M.S., Porritt, R.W., 2018. Tomographic images of slab segmentation and deformation in the greater Antilles. Geochem. Geophys. Geosyst. 19 (8), 2292–2307.

Hayes, G., Wald, D.J., Hohnson, R.L., 2012. Slab 1.0: a three-dimensional model of global subduction zone geometries. J. Geophys. Res. 117 (B01302).

Hayes, G., Moore, G., Portner, D.E., Flamme, H., Furtney, M., Smoczyk, G., 2018. Slab2- a comprehensive subduction zone geometry model. Science 382 (6410), 58–61.

Helffrich, G.R., 2000. Topography of the transition zone seismic discontinuities. Rev. Geophys. 38, 141–158.

Hosseini, K., Sigloch, K., Tsekhmistrenko, M., Zaheri, A., Nissen-Meyer, T., Igel, H., 2020. Multifrequency tomography using P, PP and P-diffracted waves. Global Mant. Struct. Geophysi. J. Int. 220 (1), 96–141.

Houser, C., Maters, G., Flanagan, M., Shearer, P., 2008. Determination and analysis of long-wavelength transition zone structure using SS precursors. Geophys. J. Int. 174, 178–194.

Isacks, B., Molnar, P., 1971. Distribution of stresses in the descending lithosphere from a global survey of focal-mechanism solutions of mantle earthquakes. Rev. Geophys. Space Phys. 9 (1), 103–174.

Ishii, T., Kojitani, H., Akaogi, M., 2011. Post-spinel transitions in pyrolite and Mg2SiO4 and akimotoite– perovskite transition in MgSiO3: precise comparison by high-pressure high-temperature experiments with multi-sample cell technique. Earth Planet. Sci. Lett. 309 (185–197), 2011.

Ito, E., Takahashi, E., 1989. Postspinel transformations in the system Mg2SiO4-Fe2SiO4 and some geophysical implications. J. Geophys. Res. Solid Earth 94 (B8), 10637–10646.

Ito, E., Akaogi, M., Topor, L., Navrotsky, A., 1990. Negative pressure-temperature slopes for reactions formign mgsio3 perovskite from calorimetry. Science 249 (4974), 1275–1278.

Jagoutz, O., Royden, L., Holt, A.F., Becker, T.W., 2015. Anomalously fast convergence of India and Eurasia caused by double subduction. Nat. Geosci. 8, 475–547.

Kaneshima, S., Kubo, T., Yoshioka, S., 2012. Geophysical and mineralogical constraints on the post-spinel transformation for the Tonga slab. Phys. Earth Planet. Inter. 196-197, 23–31.

Katsura, T., Ito, E., 1989. The system Mg_2SiO_4-Fe_2SiO_4 at high pressures and temperatures: precise determination of stabilities of olivine, modified spinel, and spinel. J. Geophys. Res. Solid Earth 94 (B11), 15663–15670.

Katsura, T., Yamada, H., Shinmei, T., Kubo, A., Ono, S., Kanzaki, M., Yoneda, A., Walter, M.J., Ito, E., Urakawa, S., Funakoshi, K., Utsumi, W., 2003. Post-spinel

transition in Mg2SiO4 determined by high P-T in-situ X-ray diffractometry. Phys. Earth Planet. Inter. 136, 11–24.
Katsura, T., Yamada, H., Nishikawa, O., Song, M., Kubo, A., Shinmei, T., Yokoshi, S., Aizawa, Y., Yoshino, T., Walter, M.J., Ito, E., Funakoshi, K.-I., 2004. Olivine-Wadsleyite transition in the system (Mg, Fe)$_2$Sio$_4$. J. Geophys. Res. Solid Earth 109, B02209. https://doi.org/10.1029/2003JB002438.
Kennett, B.L.N., Engdahl, E.R., Buland, R., 1995. Constraints on seismic velocities in the earth from traveltimes. Geophys. J. Int. 122 (1), 108–124.
Koppers, A.A.P., Becker, T.W., Jackson, M.G., Konrad, K., Müller, R.D., Romanowicz, B., Steinberger, B., Whittaker, J.M., 2021. Mantle plumes and their role in earth processes. Nat. Rev.: Earth Environ. 2, 382–401.
Lawrence, J.F., Shearer, P.M., 2006. A global study of transition zone thickness using receiver functions. J. Geophys. Res. Solid Earth 111 (B6). https://doi.org/10.1029/2005JB003973.
Lebedev, S., Chevrot, S., van der Hilst, R.D., 2002. The 660-km discontinuity within the subducting NW-Pacific lithospheric slab. Earth Planet. Sci. Lett. 205, 25–35.
Lee, C., King, S.D., 2011. Dynamic buckling of subducting slabs reconciles geological and geophysical observations. Earth Planet. Sci. Lett. 312, 360–370.
Lessing, S., Thomas, C., Rost, S., Cobden, L., Dobson, D.P., 2014. Mantle transition zone structure beneath India and Western China from migration of PP and SS precursors. Geophys. J. Int. 197, 396–413.
Lessing, S., Thomas, C., Saki, M., Schmerr, N., Vanacore, E., 2015. On the difficulties of detecting PP precursors. Geophys. J. Int. 201, 1666–1681.
Li, C., van der Hilst, R.D., Engdahl, E.R., Burdick, S., 2008. A new global model for P wave speed variations in Earth's mantle. Geochem. Geophys. Geosyst. 9 (5) https://doi.org/10.1029/2007GC001806.
Litasov, K., Ohtani, E., Sano, A., Suzuki, A., Funakoshi, K., 2005a. In situ X-ray diffraction study of post-spinel transformation in a peridotite mantle: implications for the 660-km discontinuity. Earth Planet. Sci. Lett. 238, 311–328.
Litasov, K.D., Ohtani, E., Sano, A., Suzuki, A., Funakoshi, K., 2005b. Wet subduction versus cold subduction. Geophys. Res. Lett. 32 (2005), L13312.
Liu, H., Leng, W., 2019. Plume-tree structure induced be low viscosity layers in the upper mantle. Geophys. Res. Lett. 47 e2019GL08650.
Lu, C., Grand, S.P., 2016. The effect of subducting slabs in global shear wave tomography. Geophys. J. Int. 205 (2), 1074–1085.
Lynner, C., Long, M.D., 2013. Sub-slab seismic anisotropy and mantle flow beneath the Caribbean and scotia subduction zones: effects of slab morphology and kinematics. Earth Planet. Sci. Lett. 361, 367–378.
McNamara, A.K., Zhong, S., 2004. Thermochemical structures within a spherical mantle: Superplumes or piles? J. Geophys. Res. 109 (B07402).
Miller, M.S., Levander, A., Niu, F., Li, A., 2009. Upper mantle structure beneath the Caribbean-south American plate boundary from surface wave tomography. J. Geophys. Res. Solid Earth 114 (B1).
Mohammadzaheri, A., Sigloch, K., Hosseini, K., 2021. Subducted lithosphere under South America from multifrequency P wave tomography. J. Geophys. Res. Solid Earth 126 (6) e2020JB020704.
Muirhead, K.T., Datt, R., 1976. The N-th root process applied to seismic array data. Geophys. J. Int. 47 (1), 197–210.
Obrebski, M., Allen, R.M., Xue, M., Hung, S.-H., 2010. Slab-plume interaction beneath the Pacific northwest. Geophys. Res. Lett. 37 (L14305), 1–6.
Pérez-campos, X., Clayton, R.W., 2014. Interaction of Cocos and Rivera plates with the upper-mantle transition zone underneath Central Mexico. Geophys. J. Int. 197 (3), 1763–1769.
Porritt, R.W., Becker, T.W., Monsalve, G., 2014. Seismic anisotropy and slab dynamics from *SKS* splitting recorded in Colombia. Geophys. Res. Lett. 41 (24), 8775–8783.
Portner, D.E., Rodriguez, E.E., Beck, S., Zandt, G., Scire, A., Rocha, M.P., Bianchi, M.B., Ruiz, M., Franca, G., Condori, C., Alvarado, P., 2020. Detailed structure of the subducted Nazca slab into the lower mantle derived from continent-scale teleseismic P wave tomography. J. Geophys. Res. Solid Earth 125 (5) e2019JB017884.
Pusok, A., Stegman, D., 2019. Formation and stability of same-dip double subduction systems. J. Geophys. Res. 124, 7387–7412.
Reiss, A., Thomas, C., van Driel, J., Heyn, B., 2017. A hot midmantle anomaly in the area of the Indian Ocean geoid low. Geophys. Res. Lett. 44 (13), 6702–6711.
Reiss, A., Thomas, C., Lecocq, T., 2018. Using SP precursor waves to detect upper-mantle discontinuities. Geophys. J. Int. 215 (3), 1914–1929.
Ritsema, J., Deuss, A., van Heijst, H.J., Woodhouse, J.H., 2011. S40RTS: a degree-40 shear-velocity model for the mantle from new Rayleigh wave dispersion, teleseismic traveltime and normal-mode splitting function measurements. Geophys. J. Int. 184, 1223–1236.
Rochira, F., Thomas, C., 2023. On the importance of using directional information in the search for lower mantle reflectors. Seism. Record. 3(2) (96), 104.
Rost, S., Thomas, C., 2002. Array seismology: methods and application. Rev. Geophys. 40 (3) https://doi.org/10.1029/2000RG000100, 2-1 – 2-27.
Rost, S., Thomas, C., 2009. Improving seismic resolution through array processing techniques. Surv. Geophys. 30, 271–299.
Rost, S., Weber, M., 2002. The upper mantle transition zone discontinuities in the Pacific as determined by short-period array data. Earth Planet. Sci. Lett. 204 (3–4), 347–361.
Saki, M., Thomas, C., Nippress, S., Lessing, S., 2015. Topography of upper mantle seismic discontinuities beneath the North Atlantic: the Azores, Canary and Cape Verde plumes. Earth Planet. Sci. Lett. 409, 193–202.
Saki, M., Thomas, C., Cobden, L., Abreu, R., Buchen, J., 2019. Causes for polarity reversals of PP precursor waves reflecting off the 410 km discontinuity beneath the Atlantic. Phys. Earth Planet. Inter. 286, 111–126.
Saki, M., Thomas, C., Abreu, R., 2022. Detection and modelling of strong topography of mid-mantle structures beneath the northern Atlantic. Geophys. J. Int. 229 (1), 219–234.
Sanchez-Rojas, J., Palma, M., 2014. Crustal density structure in northwestern South America derived from analysis and 3-D modeling of gravity and seismicity data. Tectonophysics 634, 97–115.
Schlaphorst, D., Melekhova, E., Jendall, J.M., Blundy, J., Latchman, J.L., 2017. Probing layered arc crust in the Lesser Antilles using receiver function. R. Soc. Open Sci. 5 (11), 180764.
Schmerr, N., Garnero, E., 2007. Upper mantle discontinuity topography from thermal and chemical heterogeneity. Science 318, 623–626.
Schmerr, N., Thomas, C., 2011. Subducted lithosphere beneath the Kuriles from migration of PP precursors. Earth Planet. Sci. Lett. 311, 101–111.
Schmerr, N., Garnero, E., McNamara, A., 2010. Deep mantle plumes and convective upwelling beneath the Pacific Ocean. Earth Planet. Sci. Lett. 294 (1–2), 143–151.
Schubert, G., Tackley, P.J., 1995. Mantle dynamics: the strong control of the spinel-perovskite transition at a depth of 600 km. J. Geodyn. 20 (4), 417–428.
Schweitzer, J., Fyen, J., Mykkeltveit, S., Kvaerna, T., 2002. Seismic arrays: in new manual of seismological observatory practice-NMSOP. IASPEI 481–532.
Shearer, P.M., Masters, G., 1992. Global mapping of topography on the 660-km discontinuity. Nature 355, 791–796.
Shim, S.H., Duffy, T.S., Shen, G., 2001. The post-spinel transformation in Mg_2SiO_4 and its relation to the 660-km seismic discontinuity. Nature 411, 571–574.
Stammler, K., 1993. Seismic handler: programmable multichannel data handler for interactive and automatic processing of seismological analysis. Comput. Geosci. 19 (2), 135–140.
Stixrude, L., 1997. Structure and sharpness of phase transitions and mantle discontinuities. J. Geophys. Res. Solid Earth 102 (B7), 14835–14852.
Stixrude, L., Lithgow-Bertelloni, C., 2011. Thermodynamics of mantle minerals – II. Phase equilibria. Geophys. J. Int. 184, 1180–1213.
Stixrude, L., Lithgow-Bertelloni, C., 2012. Geophysics of chemical heterogeneity in the mantle. Annu. Rev. Earth Planet. Sci. 40, 569–595.
Syracuse, E.M., Maceira, M., Prieto, G.A., Zhang, H., Ammon, C.J., 2016. Multiple plates subducting beneath Colombia, as illuminated by seismicity and velocity from the joint inversion of seismic and gravity data. Earth Planet. Sci. Lett. 444, 139–149.
Tackley, P.J., 2012. Dynamics and evolution of the deep mantle resulting from thermal, chemical, phase and melting effects. Earth Sci. Rev. 110, 1–25.
Thomas, C., Billen, M.I., 2009. Mantle transition zone structure along a profile in the SW Pacific: thermal and compositional variations. Geophys. J. Int. 176 (1), 113–125.
Trela, J., Gazel, E., Sobolev, A.V., Moore, L., Bizimis, M., Jicha, B., Batanova, V.G., 2017. The hottest lavas of the Phanerozoic and the survival of deep Archean reservoirs. Nat. Geosci. 10, 451–457.
van Benthem, S., Govers, R., Spakman, W., Wortel, R., 2013. Tectonic evolution and mantle structure of the Caribbean. J. Geophys. Res. Solid Earth 118 (6), 3019–3036.
van der Hilst, R., Mann, P., 1994. Tectonic implications of tomographic images of subducted lithosphere beneath northwestern South America. Geology 22 (5), 451–454.
van der Hilst, R.D., Engdahl, E.R., Spakmann, W., Nolet, G., 1991. Tomographic images of subducted lithosphere below Northwest Pacific Island arcs. 1991. Nature 353, 37–43.
van der Hilst, R.D., Widiyantoro, S., Engdahl, E.R., 1997. Evidence for deep mantle circulation from global tomography. Nature 386, 578–584.
van der Meijde, M., Marone, F., Giadini, D., van der Lee, S., 2003. Seismic evidence for water deep in Earth's upper mantle. Science 300 (5625), 1556–1558.
van Keken, P.E., Gable, C.W., 1995. The interaction of a plume with a rheological boundary: a com- parison between two and three-dimensional models. J. Geophys. Res. Solid Earth 100 (B10), 20291–20302.
Wamba, M.D., Montagner, J.-P., Romanowicz, B., 2023. Imaging deep-mantle plumbing beneath the Réunion and Comores hot spots: vertical plume conduits and horizontal ponding zones. Sci. Adv. 9 (4), 1–6.
Weidner, D.J., Wang, Y., 1998. Chemical- and Clapeyron-induced buoyancy at the 660 km discontinuity. J. Geophys. Res. Solid Earth 103 (B4), 7431–7441.
Weidner, D.J., Wang, Y., 2000. Phase transformations: Implications for mantle structure. In: Karato, S., Forte, A.M., Liebermann, R.C., Masters, G., Stixrude, L. (Eds.), Earth's Deep Interior: Mineral Physics and Tomography from the Atomic to the Global Scale, Geophysical Monograph, Ser, 117. AGU, Washington DC, USA, pp. 215–235.
Weller, O.M., Copley, A., Miller, W.G.R., Palin, R.M., Dyck, B., 2019. The relationship between mantle potential temperature and oceanic lithosphere buoyancy. Earth Planet. Sci. Lett. 518, 86–99.
Wessel, P., Smith, W.H.F., 1995. New version of the generic mapping tools released, EOS. Trans. Am. Geophys. Union 76, 329.
Wood, B.J., 1995. The effect of H2O on the 410-kilometer seismic discontinuity. Science 268, 74–76.
Yarce, J., Monsalve, G., Becker, T.W., Cardona, A., Poveda, E., Alvira, D., Ordoñez-Carmona, O., 2014. Seismological observations in northwestern South America: evidence for two subduction segments, contrasting crustal thicknesses and upper mantle flow. Tectonophysics 637, 57–67.
Ye, Y., Gu, C., Shim, S.-H., Meng, Y., Prakapenka, V., 2014. The postspinel boundary in pyrolytic compositions determined in the laser-heated anvil cell. Geophys. Res. Lett. 41 (11), 3833–3841.
Yu, C., Day, E.A., de Hoop, M.V., Campillo, M., van der Hilst, R.D., 2017. Mapping mantle transition zone discontinuities beneath the Central Pacific with array processing of SS precursors. J. Geophys. Res. 122 (12), 10364–10378.

Zhang, Q., Guo, F., Zhao, L., Wu, Y., 2017. Geodynamics of divergent double subduction: 3-D numerical modeling of a Cenozoic example in the Molucca Sea region, Indonesia. J. Geophys. Res. 122, 3977–3998.
Zhao, Q., Yao, Y., Yao, W., 2017. A troposphere tomography method considering the weighting of input information. Ann. Geophys. 35, 1327–1340.
Zhong., S., 2006. Constraints on thermochemical convection of the mantle from plume heat flux, plume excess temperature and upper mantle temperature. J. Geophys. Res. 111 (B04409).